Journal of Natural Sciences
December 2015, Vol. 3, No. 2, pp. 33-62
ISSN 2334-2943 (Print) 2334-2951 (Online)

Published by American Research Institute for Policy Development
DOI: 10.15640/jns.v3n2a3
URL: http://dx.doi.org/10.15640/jns.v3n2a3

Bridging Thermodynamic and Kinetic Processes in Electrochemically Relevant Calculated Pourbaix Diagrams

Yolanda A. Small[1]

Abstract

The transition states in kinetic processes are often experimentally elusive. Computational tools can be used to gain an atomistic perspective into these transition states. A learning tool to guide students through the complexities of the theory while gaining an appreciation for the coupling of thermodynamic and kinetic processes is explored here. A computational protocol which hinges on combining calculated free-energy profiles along proposed mechanistic pathways with electrochemically relevant Pourbaix diagrams has been proposed with the design of molecular catalysts for hydrogen production and oxidation in mind. Two experimentally characterized species are used to test the protocol; the outcome suggests interesting ways to tune a catalyst for optimal activity. This protocol can be used as either a pedagogical tool or a research directive on how to combine theoretical analysis to experimental electrochemical studies.

1. Introduction

The challenge of meeting the energy demands of the modern age while preserving environmental quality is driving a push towards finding renewable energy sources.[1-5] Fuel cells are one such target because the energy source can be garnered from solar power and the naturally abundant water supply.[6] We are exploring ways to design efficient catalysts for reversibly carrying out the water splitting process. Hydrogen production is a fundamental step in water splitting, and hydrogen oxidation is the cathodic process in a hydrogen fuel cell.[7] Hydrogenase enzymes catalyze both processes with extreme efficiency and are thus useful as a learning tool to help in the design of hydrogenase-like catalysts.[8]

[1] Department of Chemistry, York College and The Graduate Center – City University of New York, 94-20 Guy R. Brewer Blvd. Queens, New York 11451, USA. Tel: +1 718 262 2592; corresponding author: ysmall@york.cuny.edu

In this paper, computational methods are applied to explore features of catalysts, inspired by hydrogenase enzymes, and evaluate their contributions to overall catalytic ability. The role of the ligand architecture and the influence of solvent on the catalysts' ability to function in a thermodynamically realizable regime for proton-coupled electron-transfer processes are the primary focus. We adopt a systematic approach of describing a set of possible mechanistic routes for H_2 production and oxidation and characterize the intermediates in order to elucidate the most energetically favored reaction mechanism. In the vast potential energy landscape of these model systems, this approach could reveal starting structures that can be used to explore transition states at critical junctures along the reaction coordinate. Insight gained from understanding the mechanism of how these catalytic models function can be correlated with the electrochemical operating conditions of the experiments. Together, the information offers the opportunity to recommend more efficient designs. This paper is organized as follows: Section II (Background/Motivation) introduces two crystal structures and corresponding data for experimentally characterized hydrogenase-inspired model catalysts that motivated this work; Section III (Method) describes the computational approach of using free energy profiles and coupled Pourbaix diagrams as a tool for understanding the reaction mechanism and determining the electrochemically tunable aspects of catalyst design; Section IV (Results) first introduces the proposed mechanistic routes of H_2 oxidation and production and describes the intermediates. Using these intermediates as the reference compound, free-energy profiles are calculated to establish the favored mechanistic route.

Next this section summarizes the properties of calculated coupled Pourbaix diagrams which illustrate the optimal electrochemical operating regimes for the catalyst. Section V (Conclusion) summarizes the work and attempts to identify trends in the results.

2. Background / Motivation

Catalysts for hydrogen production and oxidation which utilize metal centers coordinated by diphosphine ligands with nitrogen pendent bases have been explored by several experimental groups.[9-14] A recent review summarizes a series of hydrogenase mimics utilizing nickel and cobalt transition metals.[15] These catalysts bear some structural resemblance to the active site of hydrogenase enzymes; they employ a nickel metal center as in the Ni-Fe hydrogenase, but only a single metal center at which hydrogen oxidation and production occurs. Crystal structures have been characterized for these catalysts that indicate that the nickel center is in a 4-coordinate configuration with the two diphosphine ligands, indicative of the Ni^{II} oxidation state.[10,14,16-19] The diphosphine ligands and alkyl group substituents are oriented to place nitrogen atoms at a distance of around 3.4 Å from the metal center. Fig.1.

Compound **A**, [Ni $(P^{Ph}{}_2N^{Ph}{}_2)_2(CH_3CN)](BF_4)_2$ where $P^{Ph}{}_2N^{Ph}{}_2$ is 1,3,5,7-tetraphenyl-1,5-diaza-3,7 diphosphacyclooctane, has phenyl groups attached to the phosphorous and nitrogen base sites and an explicit acetonitrile ligated to the metal center.[20,21] Compound **A** has been shown to perform best as an H_2 production catalyst. Compound **B,** [Ni $(P^{Cy}{}_2N^{Bz}{}_2)_2](BF_4)_2$, has cyclohexyl (Cy) groups on phosphorous and benzyl (Bz) groups on the nitrogen base sites and has been shown to perform best as an H_2 oxidation catalyst. However, the turnover frequency for these models is still well below that of the Ni-Fe Hydrogenase enzyme.

The natural enzyme has turnover rates of 700 s^{-1},[20,22] while compound **A** has a turnover rate of 350 s^{-1} and compound **B** has a turnover rate of 10 s^{-1}.[20,21] The availability of the experimental structural and some kinetic data offers a good opportunity for theoretical methods to be used to characterize the effect of various features, or design principles, for such catalysts, and to understand which effects are likely to have the greatest influence in the reversibility and efficiency of future designs. Using density functional theory coupled to implicit solvation schemes,[23] the free-energy profiles of proposed mechanistic routes, as well as the associated pK_a values and reduction potentials ($E_{1/2}$), have been calculated for computational models of **A** and **B**.

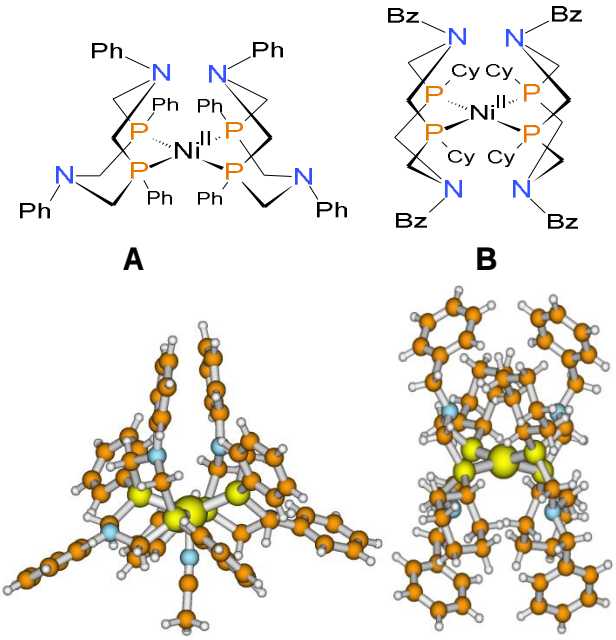

Fig. 1: Crystal structures from DuBois references are: (**A**) $[Ni(P^{Ph}{}_2N^{Ph}{}_2)_2(CH_3CN)](BF_4)_2$ $P^{Ph}{}_2N^{Ph}{}_2$ = 1,3,5,7-tetraphenyl-1,5-diaza-3,7-diphosphacyclooctane, shown to work in the H_2 production direction; and (**B**) $[Ni(P^{Cy}{}_2N^{Bz}{}_2)_2]$ shown to work in the H_2 oxidation direction.

3. Method

A. Computational Method

Density Functional Theory (DFT) was employed using the hybrid functional B3LYP[24-26] and a 6-31G(d,p) (5D, 7F) basis set in the Gaussian 03 program package.[27,28] Frequency calculations were performed at the optimized geometries to confirm minimum geometries and obtain the sum of electronic and thermal free energies for each species. Atomic charge and spin populations were calculated at the optimized geometry to confirm the oxidation state of the metal center and charge state of the ligands. To obtain the free energy of solvation, a conductor-like polarizable continuum model (CPCM)[29-32] was used to mimic the solvent, and the radii around the solute were carefully selected in such a way that charged species achieved greater interaction with the continuum through the use of smaller solvation radii.[32,33] In this case, Bondi radii[34] were used, and two parameters were adjusted to provide the lowest solvation free-energy possible for the model.[35,36]

A sphere overlap index of 0.8Å and minimum radius for added spheres of 0.5Å were used based on a series of tests using the same functional and basis set. Both adjustments result in a smaller number of added spheres. Without these adjustments, the solvation free-energy remains too high and contributes to extremely acidic pK_a values, not in the range of the known experimental values.[35,36] Lowering the solvation free-energy by adjusting these parameters calibrates our method with the experimental values of the crystal structures provided. The only solvent considered throughout this paper is acetonitrile, as used in the experimental conditions.

1. Pourbaix Diagrams Used For Proton Management.

With the goal of understanding the mechanism for H_2 oxidation and production in hydrogenase-inspired compounds, theory and experiment align to gain valuable insight into fundamental processes in these catalysts.[7,37] The Pourbaix diagram shows the thermodynamically stable form of a chemical species as a function of applied potential and pH, spanning all oxidation states accessible by redox reactions and/or acid/base reactions. The horizontal and diagonal lines plotted on the diagram are the half-potentials, i.e., the reduction potentials for all redox couples at the condition of equal concentration of the reduced and oxidized forms of the species, as a function of the solution pH. The vertical lines are the pK_a values of protonated forms of the species.

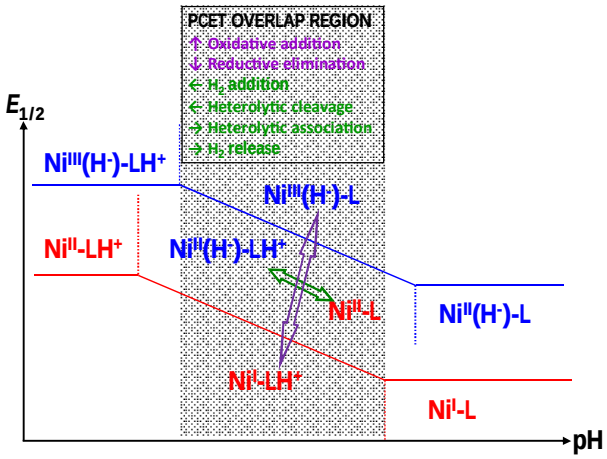

Fig. 2: Schematic illustration of coupled Pourbaix diagram. Shaded region (green) is the overlap between the PCET regions of the $N^{II/I}$ and $Ni^{III/II}(H^-)$ redox couples that must align at the same pH conditions to promote optimal catalyst performance for H_2 oxidation or production. The red and blue Pourbaix diagrams are coupled by oxidative addition or reductive elimination reactions between intermediates connected by purple double-headed arrows and heterolytic cleavage or association reactions between intermediates connected by green double-headed arrows.

For mechanisms that involve thermal reactions to produce intermediates not reached by redox processes, Pourbaix diagrams can be combined in order to provide an effective description of the process, as in Fig. 2. An example of such a thermal reaction is the rapid intramolecular proton transfer between a reduced metal center and a pendent base (i.e., reductive elimination or oxidative addition). Coupled Pourbaix diagrams can provide crucial information about the performance of a given catalyst. For example, if the mechanism operates by way of an oxidative addition reaction that transforms a Ni^I to a $Ni^{III}(H^-)$ species that is the precursor to further redox chemistry, these two species must be able to coexist at similar pH and potential. Furthermore, such a reaction would ideally have $\Delta G° = 0$. A more detailed explanation of coupled Pourbaix diagrams has been given in our previous paper.[42] More fundamental details of the method are described in the supporting information.

2. p K_a Calculation.

To be able to compare to experiments, the pK_a is calculated by constructing a thermodynamic cycle as shown in Scheme 1 and similar in approach to ref 37.[39,43]

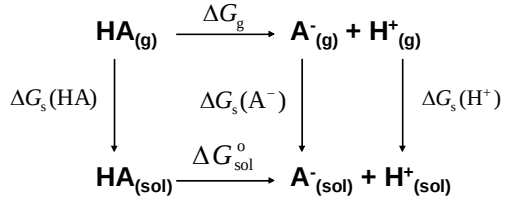

Scheme 1 General thermodynamic cycle used to calculate pK_a in acetonitrile solvent. ΔG_g is the free-energy change of the acid dissociation reaction in the gas phase where $\Delta G_g = G_g(A^-) + G_g(H^+) - G_g(HA)$ calculated with DFT at 1 atm standard state.[32,44]

$$pK_a = \frac{\Delta G^{o}_{sol} + \Delta G^{o\rightarrow *}}{2.303RT} \quad (1)$$

$$DG^{o}_{sol} = DG_g + DDG^{o}_{s} \quad (2)$$

In this construct, equations (1) and (2) are used to solve for the pK_a. ΔG^{o}_{sol} is the free-energy change of the acid dissociation reaction in solution where $\Delta\Delta G_{sol} = \Delta G_{sol}(A^-) + \Delta G_{sol}(H^+) - \Delta G_{sol}(HA)$.[45] The solvation free energy was approximated with a polarizable continuum model (PCM) solvation model.[30,39] The difference between standard states of the gas phase and solution phase is reconciled by the $\Delta G^{o\rightarrow *}$ term, taken to be 1.89 kcal/mol.[39] The solvation free-energy of the proton in acetonitrile solvent is taken from the literature to be -260.2 kcal/mol.[46] The gas-phase free energy of the proton is also taken from the literature as a value of -6.28 kcal/mol, calculated from the Sakur-Tetrode equation.[46]

3. Reduction Potential Calculation.

To calculate the standard reduction potential, a second thermodynamic cycle is constructed as shown in Scheme 2. In this construct, the Nernst equation represented by equations (3) and (4) is used to solve for the reduction potential.[46,47]

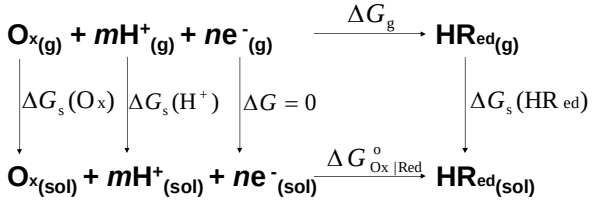

Scheme 2 General thermodynamic cycle used to calculate the reduction potential in acetonitrile solvent.

$$E^{o}_{Ox|Red} = -\frac{\left(\Delta G^{o}_{Ox|Red} - \Delta G^{o}_{RHE}\right)}{nF} \quad (3)$$

$$E = E^{o}_{Ox|Red} - \frac{RT}{nF}\ln\left(\frac{a_{Red}}{a_{Ox}}\right) - \frac{m}{n} \times 0.0591 \times pH \quad (4)$$

The absolute free energy of the normal hydrogen electrode ΔG^{o}_{RHE} in acetonitrile solution was calculated to be 4.63V and is very close to the value of 4.48V reported in ref 37. $E^{o}_{Ox|Red}$ is at unit (i.e., 1 molar) activity of oxidant and reductant (at pH 0). The reduction potential is related to the free energy that the catalyst needs to obtain *n* electrons from the normal hydrogen electrode via the reaction as in equation (5).

$$H^{+} + e^{-}_{g} \rightarrow (1/2)\, H_2 \quad (5)$$

As illustrated in the thermodynamic cycle, the number of protons is designated by *m* and the number of electrons is designated by *n*. As such, the slope of the reduction potential with respect to pH is governed by the ratio *m*/*n*.

The solvation free-energy of H_2 is calculated in acetonitrile solution using the same optimization parameters as in the model systems. The inherent error arising from the approximations introduced by the implicit solvation model is estimated to be on the order of 0.09-0.13V. This error corresponds to pK_a differences of around 2 pH units with respect to the experiments.

4. Results

A. Mechanistic Routes for H_2 Oxidation/Production.

Based on several studies on hydrogenase enzymes,[19,48] the mechanism for H_2 oxidation/production is thought to proceed via a heterolytically cleaved intermediate in which the hydride ion is attached to the metal center, forming a metal hydride, and the proton is attached to the base. We define this as Type-I H_2 bond cleavage. An alternative to this Type-I H_2 bond cleaved intermediate is the second heterolytically cleaved intermediate, which has been observed experimentally by NMR spectroscopy in some characterized catalyst models, in which both protons from the hydrogen molecule attach to different pendent base groups while the two electrons reduce the Ni^{II} metal center to Ni^{0}. We define this as Type-II H_2 bond cleavage.

The ability to reach higher or lower oxidation states of the metal and to change the basicity of the pendent base(s) can be tuned by the choice of substituent on the catalyst as shown in our previous studies.[42] In this paper, we describe possible mechanistic routes for H_2 oxidation and production which involve Type-I and Type-II H_2 bond cleaved intermediates. Analysis of the intermediates appearing in non-electrochemical and electrochemical reactions and the free-energies along these two main routes, Type-I and Type-II H_2 bond cleaved intermediates, can be linked to the experimental operating regime and offers insight into which conditions can be tuned for optimal catalyst performance.

The possible mechanistic routes for both $[Ni(P^{Ph}_2N^{Ph}_2)_2(CH_3CN)]$ and $[Ni(P^{Cy}_2N^{Bz}_2)_2]$ models have been generically summarized in Fig. 3. Starting from the bare catalyst with the metal in the 2^+ oxidation state, intermediate (**0**), upon addition of the H_2 molecule leads to two main branches considered herein. The first branch leads to intermediate (**1a**) in which a Type-II bond cleaved H_2 symmetrically protonates both nitrogen base sites and the electron reduces the metal to the Ni^0 state. In a recent publication, the Ni^0 intermediate is described as being important to intramolecular proton exchange processes in the cycle.[49] The second branch leads to intermediate (**1b**) in which a Type-I bond cleaved H_2 asymmetrically protonates the nitrogen base site and adds a hydride (H^-) to the metal center. The H_2 addition reaction from intermediates $0 \rightarrow 1$ is considered a non-electrochemical reaction and relies on a reasonable activation free energy needed to form either (**1a**) or (**1b**). The next step towards H_2 oxidation is the first of the two electrochemical reactions shown in the chemical equation $H_2 \rightarrow 2H^+ + 2e^-$.[50]

These electrochemical reactions depend on the potential applied to the electrodes and the pH of the solution. The balance between pH and potential will dictate whether the proton and electron transfers occur sequentially or in a concerted manner described as proton-coupled electron transfer (PCET). As shown in Fig. 3, if sequential electrochemical reactions occur then intermediates (**2a**), (**2b**), (**3a**), and (**3b**) can be isolated and characterized depending on whether intermediate (**1a**) or (**1b**) prevails after H_2 addition. A key factor in H_2 oxidation processes is the formation of a metal-hydride intermediate along the mechanistic route. In the case where intermediate (**1a**) is formed upon H_2 addition, an additional non-electrochemical reaction is needed from intermediate $2 \rightarrow 3$ to form the key metal-hydride intermediate. In this oxidative addition, the proton on the nitrogen base gets donated to the Ni^0 as a hydride and oxidizes the metal to Ni^{II}.

In the case where intermediate (**1b**) is formed, the oxidative addition reaction is unnecessary because the metal-hydride intermediate is already present. The next step towards H_2 oxidation is another non-electrochemical reaction from intermediate $4 \rightarrow 5$.

This reductive elimination is an intramolecular transfer where the hydride donates a proton the nitrogen base and an electron to reduce the metal from Ni^{III} to Ni^{I}. Lastly, the final step to complete H_2 oxidation is the second of the two electrochemical reactions in the process.

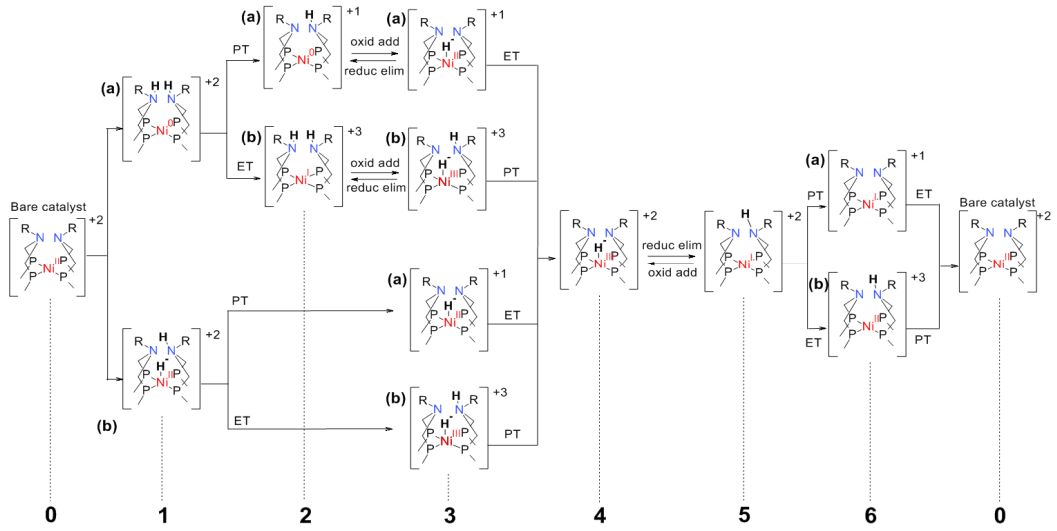

Fig. 3. Summary of mechanistic routes leading to H_2 oxidation for Nickel diphosphine model catalysts. Intermediates along this direction are classified as reaction steps producing intermediates in the order, $0 \rightarrow 1 \rightarrow 2 \rightarrow 3 \rightarrow 4 \rightarrow 5 \rightarrow 6 \rightarrow 0$. The H_2 production direction for the model is exactly the reverse process where the intermediates in the reaction steps are ordered by $0 \rightarrow 6 \rightarrow 5 \rightarrow 4 \rightarrow 3 \rightarrow 2 \rightarrow 1 \rightarrow 0$.

Again there will be a dependence on the applied potential and pH in determining if the reactions will be sequential or PCET. If sequential then intermediates (**6a**) or (**6b**) can be isolated and characterized. Catalysis in the H_2 production direction involves the $2H^+ + 2e^- \rightarrow H_2$ reaction which allows us to consider the possible mechanistic routes as the reverse of the H_2 oxidation direction previously described. For the non-electrochemical reactions, reductive elimination is the reverse of the oxidative addition reaction and H_2 release is the reverse of the H_2 addition reaction. These non-electrochemical processes are similarly governed by the kinetics of those reactions. For the electrochemical reactions, sequential or PCET processes are governed by the applied potential and pH of the reaction conditions. Therefore, for ease in describing the intermediates in these mechanistic routes, we subdivide them into two categories, those encountered in the non-electrochemical reactions and those encountered in the electrochemical reactions.

One reason is that the two categories of reactions can be controlled differently. The behavior of species involved in the non-electrochemical reactions can be controlled by knowing the structure and energy of the transition states and by tuning the ligands such that the intermediates are close in energy (i.e. $\Delta G = 0$). The species involved in the electrochemical reactions can be controlled by tuning the ligands to control the pH in which they operate and tuning the metal to control the oxidation states reached when a potential is applied. We discuss these two categories next and discuss the calculated results of $[Ni(P^{Ph}_2N^{Ph}_2)_2(CH_3CN)]$ and $[Ni(P^{Cy}_2N^{Bz}_2)_2]$ model compounds.

B. Non-electrochemical intermediates

Non-electrochemical intermediates in H_2 oxidation/production reactions are dominated by kinetic processes so it becomes important to describe the activation energy barrier in these reactions which can ultimately be compared to the rates achieved in the experiments. The two non-electrochemical intermediates for which we attempt to determine the transition states occur in Fig. 3 between intermediates $0 \rightarrow 1$, which we define as the H_2 adduct, and intermediates $4 \rightarrow 5$ which we define as a thermal reaction common to all mechanistic routes shown in Fig. 3.

1. H_2 adduct

The energy of the intermediate formed upon H_2 addition is one marker for the catalytic direction that the molecular catalyst favors. If the energy of the cleaved intermediate is favored (i.e. $-\Delta G$) with respect to the H_2 adduct, the catalyst is likely to function as an H_2 oxidation catalyst. Otherwise, the catalyst prefers scavenging available electrons and protons from the reservoir, combining them to produce H_2. As such we explored several possible conformers of the H_2 adduct and quantified their energies with respect to the Type-I or Type-II H_2 bond cleaved intermediates. This will be a useful starting structure to use for transition state searches. Beginning from different conformers of the H_2 adduct to $[Ni(P^{Cy}_2N^{Bz}_2)_2]$, three stable intermediates were located as shown in Fig. 4(i), 4(ii) and 4(iii).

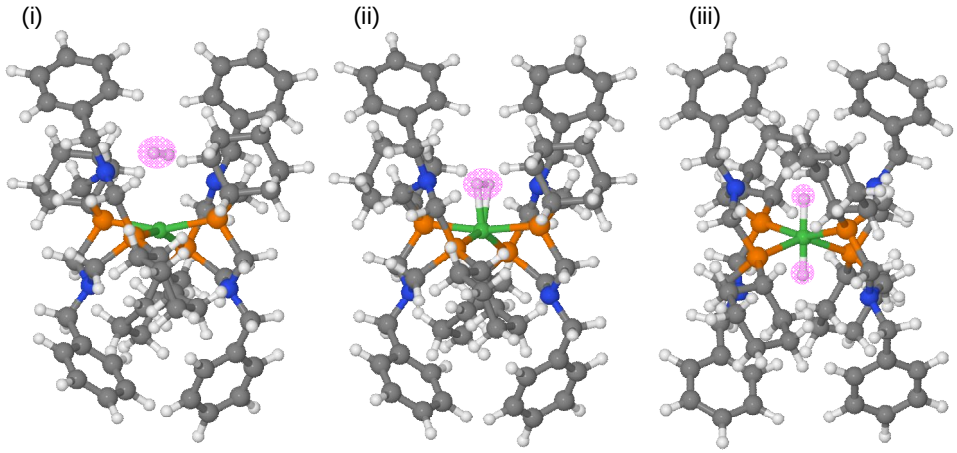

Fig. 4. Intermediates of the H_2 adduct to $[Ni(P^{Cy}_2N^{Bz}_2)_2]$ model. (i) loosely bound dihyrogen$[Ni^{II}\ldots H_2]^{2+}$; (ii) strongly bound dihydrogen $[Ni^{II}(H_2)]^{2+}$; and (iii) dihydride $[Ni^{IV}(H^-)_2]^{2+}$ trans axial the plane of the metal center and phosphorous atoms.

Table 1: Intermediates of the H_2 adduct for the $[Ni(P^{Cy}_2N^{Bz}_2)_2]$ model.

	$[Ni^{II}\ldots H_2]^{2+}$	$[Ni^{II}(H_2)]^{2+}$	$[Ni^{IV}(H^-)_2]^{2+}$ trans axial
Bond Length (Å)	**(i)**	**(ii)**	**(iii)**
H1---H2	0.8	0.8	3.0
Ni---H1	2.9	1.7	1.5
N---H1	2.4	2.4	2.8
Angle (degrees)			
P1---Ni---P2	81.5	81.2	82.8
P3---Ni---P4	81.5	81.2	82.8
P1---Ni---P3	158.6	169.2	105.1
P2---Ni---P4	156.8	141.3	105.1
H1---Ni---H2	14.6	25.8	180.0
P2---Ni---P3	102.9	102.5	149.8
P1---Ni---P4	102.9	102.4	150.0

These intermediates, labeled (i), (ii), (iii), ordered energetically from lowest to highest are $[Ni^{II}\cdots H_2]^{2+}$, $[Ni^{II}(H_2)]^{2+}$ and $[Ni^{IV}(H^-)_2]^{2+}$, respectively. Bond distances shown in Table 1 confirm the assignment of (i) as a dihydrogen loosely bound to the catalyst and (ii) as a dihydrogen strongly bound to the metal center, given the short H-H bond of around 0.8 Å.

The (i) and (ii) intermediates have similar distances from the nearest H atom to the nitrogen base sites of approximately 2.4 Å, a reasonable PT distance under the appropriate acid/base conditions.

The third H_2 adduct, (iii), is a trans axial dihydride across the plane of the metal center and the four phosphorous atoms, and has longer distances between the hydride and nitrogen of around 2.8 Å. The trans axial positioning of the hydrides across the metal phosphide plane was the only possible dihydride complex that could be found for this catalyst model given the low flexibility of the boat/boat configuration of the diphosphine rings with respect to the metal center.

On the other hand, starting from many different conformers, the H_2 adduct to $[Ni(P^{Ph}{}_2N^{Ph}{}_2)_2(CH_3CN)]$ converged to four stable intermediates, ordered energetically from lowest to highest in Fig. 5. Similar to the $[Ni(P^{Cy}{}_2N^{Bz}{}_2)_2]$ model, intermediates (i'), (ii') and (iii') are the loosely bound dihydrogen, strongly bound dihydrogen and trans axial dihydride respectively, as shown by the bond distance and angles in Table 2. However, an additional H_2 adduct found for this system is a complex with the dihydride atoms on the same face of the metal-diphosphine plane, third highest in energy from the other H_2 adducts, as shown in figure 6. For this case, both hydride ions remain on the same side of the metal phosphide plane because the boat/chair conformation of the diphosphine rings offers more flexibility at the metal center.

This dihydride intermediate $[Ni^{IV}(H^-)_2(CH_3CN)]^{2+}$ has Nickel hydride bond lengths of 1.5Å, similar to the dihydride of the $[Ni(P^{Cy}{}_2N^{Bz}{}_2)_2]$ model. Figure 6 summarizes the comparison of the energies of the various H_2 adducts with respect to the Type-II H_2 bond cleaved (**1a**) and Type-I H_2 bond cleaved (**1b**) intermediates for the two models. Figure 6(A) for the $[Ni(P^{Ph}{}_2N^{Ph}{}_2)_2(CH_3CN)]$ model shows that the dihydride intermediate (**iv'**) is nearly isoenergetic with the Type-II H_2 bond cleaved intermediate (**1a**), differing in energy by 0.06 eV. Figure 6(B) for the $[Ni(P^{Cy}{}_2N^{Bz}{}_2)_2]$ model shows that the energies of the loosely bound dihydrogen complex (i) and the Type-I H_2 bond cleaved $[Ni^{II}(H^-)\text{-}NH^+]^{2+}$ intermediate (**1b**) are nearly isoenergetic, differing by only 0.023 eV. Likewise, the energies of the dihydride (iii) and the Type-II H_2 bond cleaved intermediates (**1a**) are relatively similar, differing by 0.14 eV. The H_2 adduct nearest in energy to the Type-I or Type-II H_2 bond cleaved species is a good starting point for locating the transition state of this initial step and efforts are underway in this search. The trend in Figure 6 shows that formation of the Type-II H_2 bond cleaved intermediate (**1a**) will likely be preceded by a dihydride intermediate, and similarly, formation of the Type-I H_2 bond cleaved intermediate (**1b**) will likely be preceded by the dihydrogen complex.

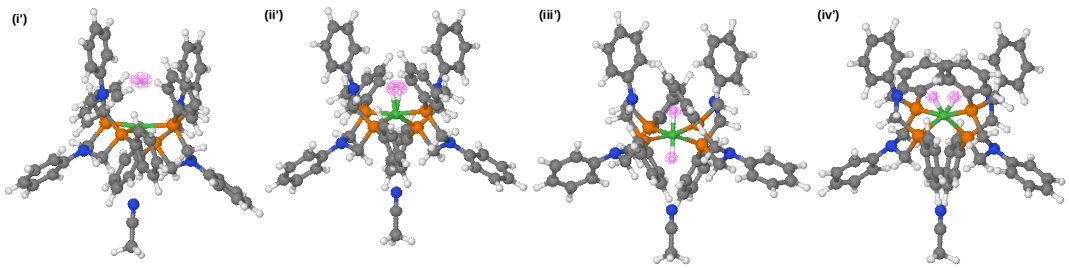

Fig. 5: Intermediates of the H_2 adduct to $[Ni(P^{Ph}{}_2N^{Ph}{}_2)_2(CH_3CN)]$ model. (I') loosely bound dihydrogen $[Ni^{II}\ldots H_2]^{2+}$; (ii') strongly bound dihydrogen $[Ni^{II}(H_2)]^{2+}$; (iii') trans axial dihydride $[Ni^{IV}(H^-)_2]^{2+}$ and (iv') $[Ni^{IV}(H^-)_2]^{2+}$ dihydride intermediate.

Table 2: Intermediates of the H_2 adduct for the $[Ni(P^{Ph}{}_2N^{Ph}{}_2)_2(CH_3CN)]$ model ordered energetically from lowest to highest.

	$[Ni^{II}\ldots H_2]^{2+}$	$[Ni^{II}(H_2)]^{2+}$	$[Ni^{IV}(H^-)_2]^{2+}$	$[Ni^{IV}(H^-)_2]^{2+}$ trans axial
Bond Length (Å)	**(i')**	**(ii')**	**(iv')**	**(iii')**
H1---H2	0.8	0.8	1.9	3.0
Ni---H1	2.8	1.8	1.5	1.5
N---H1	2.5	2.5	2.2	2.6
$Ni\text{---}NCCH_3$	4.8	4.8	5.8	4.6
Angle (degrees)				
P1---Ni---P2	83.5	83.6	84.8	84.1
P3---Ni---P4	83.6	83.5	84.8	84.1
P1---Ni---P3	171.7	171.7	161.1	150.9
P2---Ni---P4	137.8	137.8	109.3	153.4
H1---Ni---H2	16.4	25.6	81.4	180.0
P2---Ni---P3	99.6	99.3	106.3	102.6
P1---Ni---P4	99.3	99.6	106.3	102.6

The stability of these H_2 adduct intermediates, as confirmed by gas phase frequency calculations, may offer insight into the nature of the transition state needed to reach the Type-I or Type-II H_2 bond cleaved intermediate.

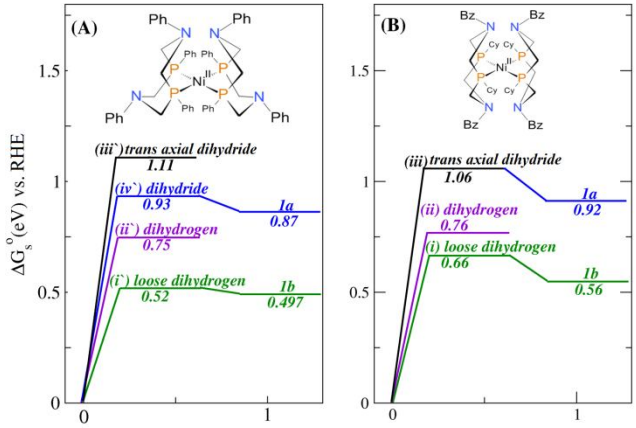

Fig. 6. Energetics of the H_2 adduct with respect to the Type-I and Type-II H_2 bond cleaved intermediates. Energy differences are taken with respect to the free catalyst and H_2.

2. Thermal reaction common to all mechanistic routes – Intermediates and Transition States

The second non-electrochemical reaction along the H_2 production mechanistic route is an oxidative addition involving intermediates 5 → 4 of Fig. 3, the reverse of which is considered a reductive elimination. In an optimal catalyst, the free-energy for this step should be nearly isoenergetic (i.e. $\Delta G \approx 0$) and the free-energy of activation ($\Delta G^{\neq}$) should be low. We calculate the transition state at this reaction step to understand the structure and energetics of the reacting species. Fig. 7 shows the structures of the transition states characterized by the negative eigenvalue of the hessian matrix along the donor/acceptor mode between the metal center and the nitrogen base site of compounds **A** and **B**. Distances and angles of the reacting species are shown in table 3 for the $[Ni(P^{Ph}{}_2N^{Ph}{}_2)_2(CH_3CN)]$ model and table 4 for the $[Ni(P^{Cy}{}_2N^{Bz}{}_2)_2]$ model. The tables show that the transferring proton is approximately midway between the donor atom (Ni) and the acceptor atom (N) for both compounds.

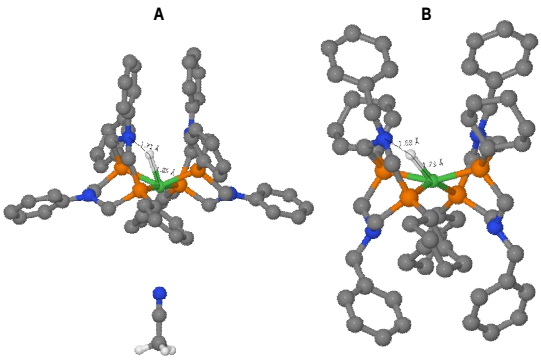

Fig. 7. Oxidative addition transition state, between intermediates 5 → 4, for compound **A**, [Ni($P^{Ph}_2N^{Ph}_2$)$_2$(CH_3CN)] model and compound **B**, [Ni($P^{Cy}_2N^{Bz}_2$)$_2$] model. The transferring proton is midway between the donor atom (Ni) and acceptor atom (N).

Table 3 Oxidative Addition 5 → 4 in the [Ni($P^{Ph}_2N^{Ph}_2$)$_2$(CH_3CN)] model for H_2 production.

	Intermediate (4)	**Transition State**	**Intermediate (5)**
Bond Length (Å)	**P**	**TS**	**R**
Ni---H1	1.46	1.67	2.86
N---H1	2.31	1.46	1.03
Ni---NCCH$_3$	5.78	5.75	5.47
frequency of Ni—H—N mode (cm^{-1})	---	921.01i	---
Angle (degrees)			
P1---Ni---P2	86.07	82.52	85.51
P3---Ni---P4	83.54	82.92	86.44
P1---Ni---P3	159.78	157.99	145.20
P2---Ni---P4	109.77	112.92	121.54
P2---Ni---P3	107.39	105.56	111.98
P1---Ni---P4	106.49	106.54	110.48
ΔG^{o}_{s} (R & P) (eV)	0.32		0.00
$\Delta G^{\neq}$ (TS) (eV) relative to reactant		0.60	

In the [Ni($P^{Ph}_2N^{Ph}_2$)$_2$(CH_3CN)] model, the flexibility of the boat/chair configuration allows for large rearrangements of the angles around the diphosphine plane. For example, the P1---Ni---P3 and P2---Ni---P4 angles undergo the largest changes between the reactant (R), transition state (TS) and product (P) configurations, shown in table 3. The constraint of the boat/boat configuration in the [Ni($P^{Cy}_2N^{Bz}_2$)$_2$] model shows much less rearrangement of the angles between the (R), (TS) and (P), as seen in Table 4.

Comparing the transition states of the two compounds, Table 3, shows that the P---Ni---P angles of the (TS) have more product character than reactant character while Table 4 shows the opposite behavior for the [Ni($P^{Cy}_2N^{Bz}_2$)$_2$] model. In other words, both transition states have diphosphine bite angles similar to intermediate (**4**) of Fig. 3. This implies that the barrier for oxidative addition will be higher than the barrier for reductive elimination. Given nature of the transition state structurally appears to be associated with the bite angle and is therefore impacted by the amount of steric bulk from the ligands. As such, consideration should be given to designing the catalyst with some flexibility in the first coordination shell to the metal center.

Table 4: Reductive Elimination 4 → 5 in the [Ni($P^{Cy}_2N^{Bz}_2$)$_2$] model for H_2 oxidation.

	Intermediate (4)	**Transition State**	**Intermediate (5)**
Bond Length (Å)	**R**	**TS**	**P**
Ni---H1	1.46	1.74	2.91
N---H1	2.79	1.68	1.03
frequency of Ni—H—N mode (cm^{-1})	---	654.89i	---
Angle (degrees)			
P1---Ni---P2	82.07	82.06	82.49
P3---Ni---P4	82.06	82.07	83.62
P1---Ni---P3	152.66	152.66	147.20
P2---Ni---P4	147.62	147.02	146.35
P2---Ni---P3	105.80	105.79	105.94
P1---Ni---P4	105.79	105.80	107.08
ΔG^o_s (R & P) (eV)	0.00		-1.07
$\Delta G^{\neq}$ (TS) (eV) relative to reactant		0.48	

C. Electrochemical intermediates

The second category of intermediates along H_2 oxidation/production mechanistic routes are the electrochemical intermediates, those involving redox and acid/base reactions. In Fig. 3, the first of the two electrochemical steps in the $2H^+ + 2e^- \rightarrow H_2$ reaction occurs between intermediates (**1**) and (**4**), and the second occurs between intermediates (**5**) and (**0**). The electrochemical reactions can be sequential PT and ET or concerted PCET. If sequential, the order of ET followed by PT or vice versa is not easily determined *a priori* and depends on the pH of the experimental conditions, along with the potential needed to reach redox species along the mechanistic route.

Therefore, we calculate the free-energy profile along various mechanistic routes to understand which species are energetically likely to dominate.

D. Free-energy Comparison of Type-I and Type-II H_2 bond cleaved mechanistic routes

The characterized catalyst (**A**), has been shown to operate as an H_2 production catalyst while (**B**) has been shown to operate as an H_2 oxidation catalyst. As such, we explore the free-energy profiles of each calculated model catalyst along the catalytic direction in which they are thought to operate. An important component in determining the mechanism is the formation of the H_2 adduct as the first step in the H_2 oxidation direction. As such, this importance is highlighted by using a proposed adduct as the reference compound in the free energy profiles, instead of the bare catalyst plus a gas phase hydrogen molecule. In doing so, the magnitude of the free energy of key steps (i.e. PCET and electrochemical steps) is similar to the corresponding free energy steps of our previous paper.[42] Efforts are underway to determine the true transition state of these key steps.

1. H_2 Production in $[Ni(P^{Ph}_2N^{Ph}_2)_2(CH_3CN)]$.

Free-energy calculations on the $[Ni(P^{Ph}_2N^{Ph}_2)_2(CH_3CN)]$ model were performed, and will be discussed here in the catalytic direction for H_2 production. Figure 8 illustrates the calculated free-energy versus the reversible hydrogen electrode (RHE) along the proposed H_2 production mechanistic routes at pH = 0. Intermediates along the reaction coordinate, emphasizing the distinction between the two Type-II H_2 bond cleaved (Paths 1 and 2) and two Type-I H_2 bond cleaved (Paths 3 and 4) routes are explained in the caption.

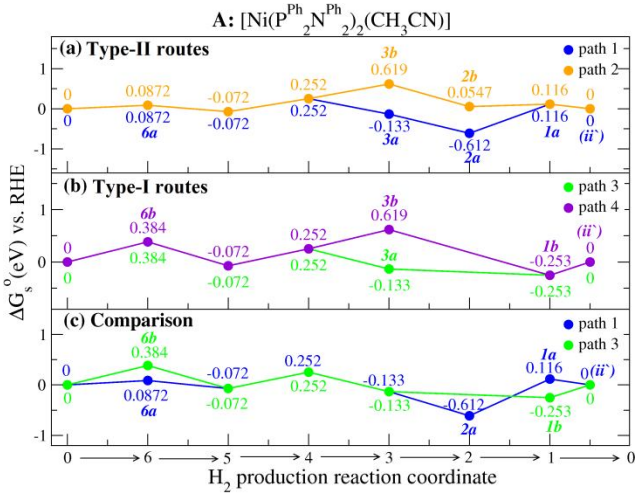

Fig. 8: Summary of mechanistic routes leading to H_2 production of $[Ni(P^{Ph}{}_2N^{Ph}{}_2)_2(CH_3CN)]$ at conditions of pH = 0. Energy differences are taken with respect to the first point, the H_2 adduct, and normalized to the reversible hydrogen electrode (RHE). Intermediates involved in each route are:

Type-II Path 1(blue): **0** → **6a** → **5** → **4** → **3a** → **2a** → **1a** → **0**.
Type-II Path 2(orange): **0** → **6a** → **5** → **4** → **3b** → **2b** → **1a** → **0**.
Type-I Path 3(green): **0** → **6b** → **5** → **4** → **3a** → **1b** → **0**.
Type-I Path 4(purple): **0** → **6b** → **5** → **4** → **3b** → **1b** → **0**.

In figure 8, the Type-II H_2 bond cleaved routes are the ones in which intermediate (**1a**) is involved in the mechanism and Type-I H_2 bond cleaved routes involve intermediate (**1b**). Panel (a) illustrates that when the two Type-II H_2 bond cleaved routes are compared, path 1 (blue), which follows intermediates **0** → **6a** → **5** → **4** → **3a** → **2a** → **1a** → **0**, is a lower energy route than path 2 (orange). The Ni^0-NH^+ (**2a**) and $Ni^{II}(H^-)$-N (**3a**) are lower in energy than ^+HN-Ni^I-NH^+ (**2b**) and $Ni^{III}(H^-)$-NH^+ (**3b**).

Panel (b) illustrates that when the Type-I H_2 bond cleaved routes are compared, path 3 (green) which follows intermediates **0** → **6b** → **5** → **4** → **3a** → **1b** → **0**, is a lower energy route than path 4 (purple). Again, the difference here is that $Ni^{II}(H^-)$-N (**3a**) is lower in energy than $Ni^{III}(H^-)$-NH^+ (**3b**). Panel (c) then compares the lowest energy route for both Type-I and Type-II H_2 bond cleaved routes, paths 1 and 3, and is a key feature in this energy analysis. The comparison shows that the first electrochemical step, involving intermediates 0 → 5 is nearly isoenergetic. Viability of this first electrochemical step becomes important for the discussion in Section IV C about the appropriate pH regime at which the experiment should be operated.

The subsequent electrochemical step leads to the $[Ni^{I}\text{-}NH^{+}]^{2+}$ reduced metal, protonated base defined as intermediate (**5**). If PCET conditions prevail, then intermediate (**6**) is not observed, otherwise intermediate (**6a**) would be favored. The oxidative addition that follows, common to all four proposed mechanistic routes, in which the base loses the proton to the metal center as a hydride forming the $[Ni^{III}(H^{-})\text{-}N]^{2+}$ intermediate (**4**)**,** has an associated free-energy change of 0.324 eV (7.47 kcal/mol). The second electrochemical reaction involving intermediates 4 → 1, show significant deviation between Type-I and Type-II H_2 bond cleaved routes. Focusing on the H_2 adduct that is formed in intermediate **1**, before release of the H_2 molecule, intermediate 1a is 0.369 eV higher in energy than intermediate (**1b**). However, since the intermediate (**1a**) is higher in energy than the dihydrogen complex (iii) then H_2 release is favored, making this route consistent with the experimentally characterized results of the H_2 production catalyst. The dihydrogen H_2 adduct was chosen as the reference compound for this comparison.

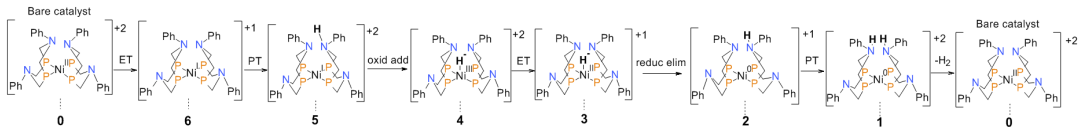

Fig. 9. Type-II H_2 bond cleaved path 1 for H_2 production of the $[Ni(P^{Ph}{}_2N^{Ph}{}_2)_2(CH_3CN)]$ model catalyst. The intermediates along this Path are **0 → 6a → 5 → 4 → 3a→ 2a → 1a → 0.**

Fig. 9 summarizes the Type-II H_2 bond cleaved mechanistic route 1 for the $[Ni(P^{Ph}{}_2N^{Ph}{}_2)_2(CH_3CN)]$ model. Under the appropriate pH conditions, a proton from the solution can attach to the catalyst at a nitrogen base site (**6b**), or an electron from an applied potential can reduce the metal center, from Ni^{II} to Ni^{I} (**6a**). Depending on whether intermediate (**6a**) or (**6b**) is formed, a subsequent electron transfer (ET) or proton transfer (PT) leads to the reduced metal with a protonated base, intermediate (**5**). The increased basicity of the metal center then causes the proton to transfer from the pendent base to the metal to form the metal-hydride, intermediate (**4**), through an oxidative addition reaction (Fig. 3, step 5 → 4).

The next step (Fig. 3, step 4 → 3), is again determined by the pH of the solution or the applied potential. If the pH allows for the availability of protons, the base becomes protonated, forming the metal-hydride with a protonated base (**3b**). Otherwise, an appropriate applied potential forms the reduced metal-hydride (**3a**). Of the two intermediates formed in step 4 → 3, (**3a**) and (**3b**), each has two alternatives along the reaction coordinate to H_2 production. If the reduced metal-hydride (**3a**) is formed, it can undergo PT immediately or as a second step after reductive elimination.

If the PT from the solution to the catalyst is favored, the Type-I H_2 bond cleaved intermediate (**1b**) is formed. If reductive elimination is favored, the hydride transfers from the metal to form a proton on the pendent base as intermediate (**2a**). Then under the appropriate pH conditions, a second pendent base becomes protonated forming the Type-II H_2 bond cleaved intermediate (**1a**). If the metal-hydride with the protonated base, intermediate (**3b**), is formed, it can either undergo a one-electron reduction immediately or as a second step after reductive elimination. If the reduction occurs immediately, the Type-I H_2 bond cleaved intermediate $[Ni^{II}(H^-)\text{-}NH^+]^{2+}$ intermediate (**1b**) is formed. If the reduction occurs as a second step, reductive elimination forms $[^+HN\text{-}Ni^{I}\text{-}NH^+]^{3+}$ as intermediate (**2b**) first, then forms the Type-II H_2 bond cleaved $[^+HN\text{-}Ni^{0}\text{-}NH^+]^{2+}$ as intermediate (**1a**). In the last step 0 → 1, the two hydrogen ions on the molecular catalyst combine with two electrons from the metal to release an H_2 molecule.

2. H_2 Oxidation in $[Ni(P^{Cy}_2N^{Bz}_2)_2]$.

Free energy calculations of similar Type-I and Type-II H_2 bond cleaved pathways in the catalytic direction for H_2 oxidation with the $[Ni(P^{Cy}_2N^{Bz}_2)_2]$ model were performed. Experimentally, the $[Ni(P^{Cy}_2N^{Bz}_2)_2]$ catalyst was observed to favor H_2 oxidation, so here we explore comparisons to the experimental system in that catalytic direction. Figure 10 shows the calculated free-energy profile of this model at pH = 0.

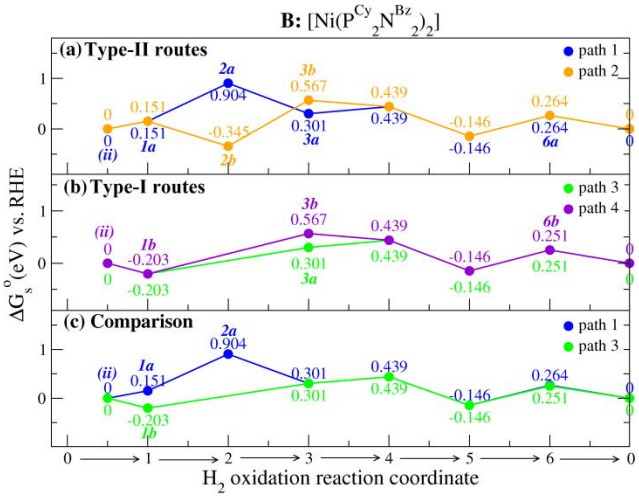

Fig. 10. Summary of mechanistic pathways leading to H_2 oxidation with the $[Ni(P^{Cy}_2N^{Bz}_2)_2]$ model at conditions of pH = 0. Energy differences are taken with respect to the first point and normalized to the reversible hydrogen electrode (RHE). Intermediates involved in each route are:

Type-II Path 1 (blue): **0** → **1a** → **2a** → **3a** → **4** → **5** → **6a** → **0**.
Type-II Path 2 (orange): **0** → **1a** → **2b** → **3b** → **4** → **5** → **6a** → **0**.
Type-I Path 3 (green): **0** → **1b** → **3a** → **4** → **5** → **6b** → **0**.
Type-I Path 4 (purple): **0** → **1b** → **3b** → **4** → **5** → **6b** → **0**.

In figure 10, the reference compound for which the energies are plotted is the dihydrogen adduct (ii), chosen for its low energy stability compared to the other calculated H_2 adducts. Panel (a) shows that the Type-II H_2 bond cleaved intermediate (1a) is 0.151 eV (3.48 kcal/mol) higher in energy than the H_2 adduct. The first electrochemical reaction follows, between intermediates 1 → 4. In this model, special attention is paid to intermediates 1a and 3a because these have both been observed with NMR spectroscopy using the characterized compounds.[21] Following the route of the NMR observed intermediates, path 1 (blue) traverses intermediates **0** → **1a** → **2a** → **3a** → **4** → **5** → **6a** → **0**. However, intermediate (**2a**) is 0.753 eV (17.37 kcal/mol) higher in energy than intermediates (**1a**).

The next step is a non-electrochemical, reductive elimination reaction, consistent in all four mechanistic routes between intermediate 4 → 5. The energy of which is downhill by 0.585 eV (13.49 kcal/mol). The second electrochemical reaction occurs between intermediate 5 → 0. Panel (b) shows that the Type-I H_2 bond cleaved intermediate (1b) is -0.203 eV (4.68 kcal/mol) lower in energy than the H_2 adduct reference compound which is consistent with this model as an H2 oxidation catalyst. In the next electrochemical reaction between 1 → 4, if PCET conditions prevail, then intermediate 3 is not observed, otherwise intermediate (3a) would be favored. A schematic description of this energetically favored Type-I H_2 bond cleaved Path 4 is shown below in Fig. 11.

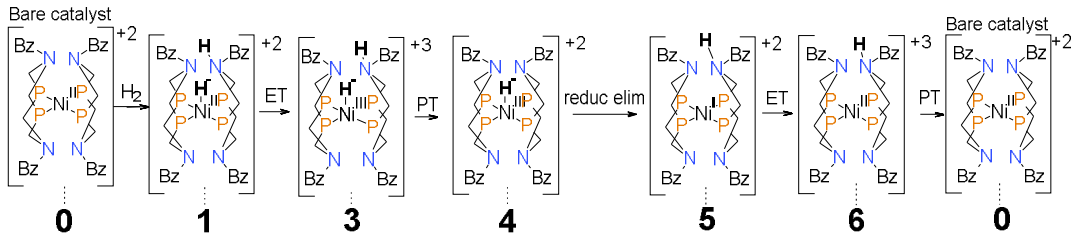

Fig. 11. Energetically favored Type-I H_2 bond cleaved Path 4 for H_2 oxidation of the $[Ni(P^{Cy}_2N^{Bz}_2)_2]$ model catalyst. The intermediates along this Path are **0** → **1b** → **3b** → **4** → **5** → **6b** → **0**.

C. Electrochemical perspective from calculated Pourbaix diagrams

One criterion for molecular catalyst design is energy matching in the non-electrochemical reaction steps. However, an additional condition to improve the efficiency of the catalyst is to control the electrochemical reactions so that the energy cost of sequential proton and electron transfer is circumvented by steering the reduction to proceed by PCET.

The goal then becomes to align all intermediates involved in the non-electrochemical reaction steps such that they are available at similar pH ranges. Hence, for the electrochemical reactions, an applied potential, at a pH, will facilitate the most efficient mechanistic route due to the availability of the most relevant species. We demonstrate this idea using the coupled Pourbaix diagram, a plot of potential versus pH where the identity of the various species has been described in the methods section above. A schematic of an expanded Pourbaix diagram illustrating all intermediates in both Type-I and Type-II H_2 bond cleaved routes is shown in Fig. 12.

The Type-II H_2 bond cleaved route shown in purple arrows in Fig. 12 is expanded schematically in Fig. 13. The ideal, most efficient mechanism would involve only PCET reactions which overlap in the pH ranges of the proton-coupled electron-transfer steps, **$PCET_{12}$**, **$PCET_{34}$** and **$PCET_{56}$**, and occur at similar potentials. The schematic Pourbaix diagram in Fig. 12 is broadly applicable to both catalysts models.

Having mapped out two relevant mechanistic routes, Type-I and Type-II H_2 bond cleaved, of these molecular catalyst models, a connection must be made to the operational pH and potential where the intermediates are accessible. We turn to the calculated coupled Pourbaix diagrams to make this necessary connection and attempt to draw correlations to the operational regimes used in the experimental setup. Fig. 14 is the coupled Pourbaix diagram of model $[Ni(P^{Cy}_2N^{Bz}_2)_2]$.

Intermediates involved in the Type-II H_2 bond cleaved routes are shaded in purple, and intermediates involved in the Type-I H_2 bond cleaved routes are shaded in green. pK_a's for the H_2 adducts correspond to the single deprotonation of the (i), (ii) and (iii) intermediates to $[Ni^{II}(H^-)\text{-}N]$.

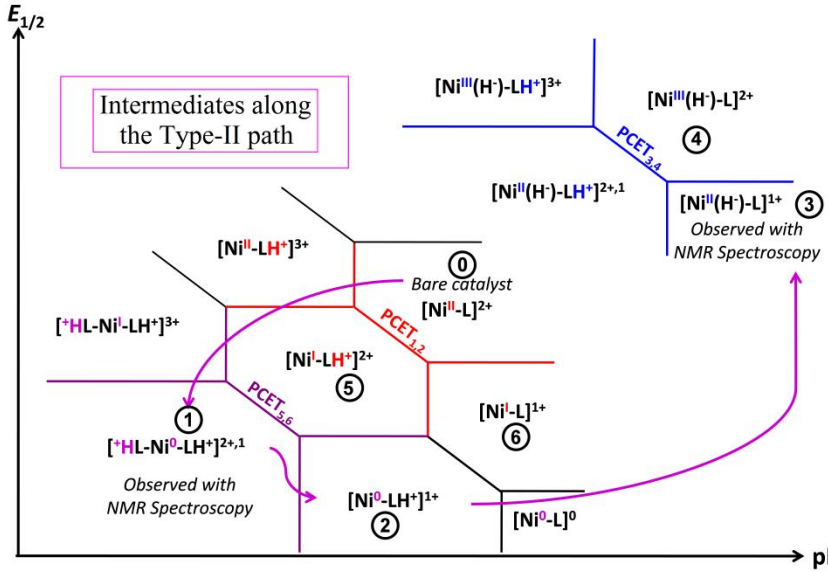

Fig. 12. Schematic of an expanded coupled Pourbaix diagram. Red lines signify the Ni^{II}/Ni^{I} couple, blue lines are the $Ni^{III/II}(H\text{-})$ couple, and purple lines are the $Ni^{I/0}$ couple. Numbered intermediates followed by purple arrows travel along the Type-II H_2 bond cleaved pathway. The intermediates labeled with circled numbers follow the Type-II H_2 bond cleaved pathway as an illustration that free-energy mechanistic routes can be mapped onto the Pourbaix diagram at a way to interpret findings from electrochemistry experiments.

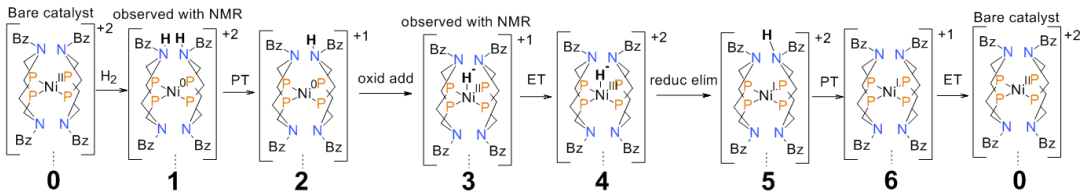

Fig. 13. Type-II H_2 bond cleaved pathway of H_2 oxidation with $[Ni(P^{Cy}_2N^{Bz}_2)_2]$ model.

Focusing first on the PCET overlap region highlighted in purple which represents the Type-II H_2 bond cleaved route, the results show that this route operates in a basic region of the pH scale and with relatively large overpotentials. Interestingly, the experiment is performed in the presence of triethylamine, a strong base buffer, which could explain why the $[{}^+HN\text{-}Ni^0\text{-}NH^+]$ intermediate is observed by NMR spectroscopy under these basic conditions. Now focusing on the PCET overlap region highlighted in green, representing the Type-I H_2 bond cleaved route, the result shows that this route operates in an acidic region of the pH scale with much lower overpotentials than the Type-II H_2 bond cleaved route.

Interestingly, the H_2 adduct represented by (ii) and (iii) in Fig. 14 falls within this pH range which is consistent with the similarity in energy to the Type-I H_2 bond cleaved intermediate. Comparing the operating regimes of both Type-I and Type-II H_2 bond cleaved routes, this Pourbaix diagram of $[Ni(P^{Cy}_2N^{Bz}_2)_2]$, indicates that if the solution can be tuned to more acidic conditions, the intermediates reached will traverse a lower energy, thus a more favorable mechanistic route.

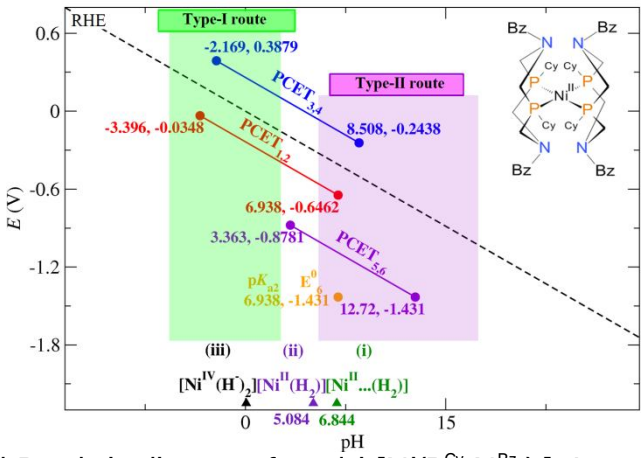

Fig. 14. Coupled Pourbaix diagram of model $[Ni(P^{Cy}_2N^{Bz}_2)_2]$. Intermediates involved in the Type-II H_2 bond cleaved pathway are shaded in purple, and intermediates involved in the Type-I H_2 bond cleaved pathway are shaded in green.

Figure 15 is the coupled Pourbaix diagram of model $[Ni(P^{Ph}_2N^{Ph}_2)_2(CH_3CN)]$. Focusing on the PCET overlap region highlighted in purple in Fig. 15 which represents the Type-II H_2 bond cleaved route, a largely acidic pH range is involved with accompanying large overpotentials. In this case, the experiment is performed in the presence of triflic acid, which correlates with the strongly acidic pH range calculated. Unlike the $[Ni(P^{Cy}_2N^{Bz}_2)_2]$ case, this case appears to be more difficult to disentangle. From the free-energy profiles, the favored mechanism for this case appears to be along the Type-I H_2 bond cleaved pathway because of the 0.354 eV lower energy of the Type-I H_2 bond cleaved intermediate. However, the Type-I H_2 bond cleaved route falls in a narrow, even more acidic region of the Pourbaix diagram but equally close to the acidic region of the Type-II H_2 bond cleaved route, although with much lower overpotential. It may be that under the acidic conditions required by both routes, PCET reactions dominate and optimal conditions for the reactions prevail.

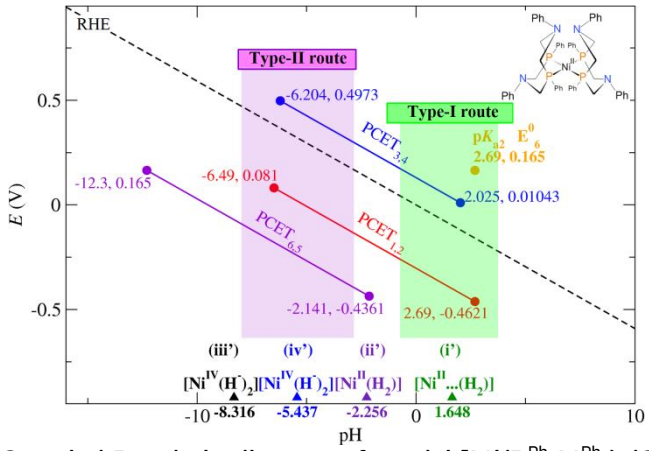

Fig. 15: Coupled Pourbaix diagram of model $[Ni(P^{Ph}_2N^{Ph}_2)_2(CH_3CN)]$.

Comparing the Pourbaix diagrams of this $[Ni(P^{Ph}_2N^{Ph}_2)_2(CH_3CN)]$ model and the previous $[Ni(P^{Cy}_2N^{Bz}_2)_2]$ model, lower potentials are needed to drive the reaction in this case and may be one contributing factor to the higher turnover frequency (TOF) of 350 s^{-1} of this catalyst as opposed to the TOF of 10 s^{-1} of the previous one. The other contributing factor being the lower change in free-energy of the oxidative addition reaction involving intermediates 5⟶ 4.

5. Discussion

In our previous paper[42], explicit emphasis was placed on matching the pK_a's of intermediates 4 & 5 (the oxidative addition step) such that the free energy of this step is thermoneutral in an ideal catalyst. Our exploration of these actual catalysts shows that there are pK_a regions of overlap for each catalyst, favoring the Type-II route. While the pK_a's overlap, the reduction potentials do not and may be a source of explanation for why these two catalysts have less than ideal turnover frequencies in their H_2 oxidation/reduction directions. The pK_a's for intermediates 4 and 5 are shown in Figures 14 and 15. While the previous work also postulated a second reduction to the Ni^0 species before the oxidative addition step, this was not observed for these real catalyst systems. In fact, we show the calculated pK_a of the Ni^0 species in Figures 14 and 15 (labeled in purple as the intermediates around **$PCET_{56}$**).

One of the strengths of the Pourbaix diagram is the opportunity to explore the mechanism in terms of the pH dependence of various routes. So far the results have presented the simple case, at pH = 0 conditions, of proton transfers being coupled to electron transfers in what is usually defined as intermolecular PCET.

However, a second, more complex process can be considered involving the coupling of oxidative additions to electron or proton transfers in a way that is traditionally defined as intramolecular PCET.

One paper argues that B3LYP is not in qualitative agreement with coupled-cluster expansion calculations on a model system of the nickle-diphosphine compound.[51] The choice of using DFT with a B3LYP functional for these calculations is based on seeking a qualitative understanding of how Pourbaix diagrams can be used to design molecular catalysts at the low computational cost of calculating pK_a's and reduction potentials of the full system, not a truncated model.

6. Conclusion

In search of renewable energy sources as a way of preserving the environment, nature's energy producers have become an attractive instructor. Hydrogenase enzymes, for example, are capable of turning over hydrogen at high rates using readily available and cost effective nickel and iron metals. While recognizing the complexity with which hydrogenases function, a few design features have been taken as a start towards building molecular catalysts which can function at comparable efficiencies. Experimentalists have characterized such compounds, two of which we chose to model in this paper, one for H_2 oxidation and the other for H_2 production. Using these models, we explored three aspects of catalytic function which can influence the choices made in designing the catalyst. The goal is to elucidate how to tune design features on the catalyst to improve efficiency, and to formulate a computational protocol which predicts how the changes ultimately affect catalyst behavior. By first mapping the free energy along a proposed reaction coordinate, we illustrate that we can decipher the mechanistic routes of the characterized catalyst and project ways to improve the catalyst by designing it to traverse more favorable routes. We then target the H_2 adduct as a critical intermediate by which the pathway can be controlled and suggest design features that coerce the catalyst into forming certain low energy intermediates.

Lastly, we correlate the free-energy routes with electrochemical mapping of the intermediates as a way to project optimal electrochemical conditions for improving catalyst behavior.

The key result from analyzing the free-energy profiles is that the heterolytic route is favored for both models, $[Ni(P^{Ph}_2N^{Ph}_2)_2(CH_3CN)]$ and $[Ni(P^{Cy}_2N^{Bz}_2)_2]$. This suggests that using ligands to make one of the two nitrogens in the upper plane of the catalyst more basic than the other can bias the reaction to reach the heterolytically cleaved intermediate. When both nitrogens have the same ligand, homolytic cleavage is more difficult to avoid.

The synthetic challenge of course becomes how to construct a catalyst with an asymmetric [Ni($P^{Ph}N^{Ph}$) ($P^{Ph}N^{Bz}$)] configuration. However, if this can be overcome, this new asymmetric catalyst may traverse the optimal heterolytically cleaved route. In analyzing the H_2 adduct intermediate, structure appears to have a large contribution in controlling whether the homolytic or heterolytic intermediate is formed. Formation of a loosely bound dihydrogen complex is nearly isoenergetic with the heterolytically cleaved intermediate and is best achieved by the complex that has diphosphine rings in the boat/boat configuration. Lastly, since potential is proportional to the free-energy, lower potentials correlate with smaller cost in free-energy. From the perspective of the Pourbaix diagrams, the results indicate that lower potentials are needed in acidic pH regions. Thus, if the asymmetric catalyst can be stabilized in acidic solution through the phenyl ligands, all optimal conditions should prevail.

While concepts of proton management have been considered by many investigators in the catalysis community,[52] we are unaware of another study which hinges on the connection between free-energy profiles and Pourbaix diagrams as a tool to design more efficient H_2 oxidation and production catalysts. Our paper is the second in this direction and hopes to gain greater appeal based on the electrochemical insight that it offers.

Further studies of this nature will of course rely on the availability of experimental data in the initial stages. However, the outcome of this study shows great promise in the future of designing efficient catalysts having a larger electrochemical component.

Acknowledgements

The work at BNL was supported by DOE under contract DE-AC02-98CH10886 (Division of Chemical Sciences and its Scientific User Facilities Division). This research utilized resources at the New York Center for Computational Sciences (NYCCS) at Stony Brook University/Brookhaven National Laboratory which was supported by the U.S. Department of Energy under Contract No. DE-AC02-98CH10886 and by the State of New York, and at the BNL Center for Functional Nanomaterials (CFN).

References

Arnold, F. H. Nature 2001, 409, 253-257.
Cortright, R. D.; Davda, R. R.; Dumesic, J. A. Nature 2002, 418, 964-967.
Kamat, P. V. Journal of Physical Chemistry C 2007, 111, 2834-2860.
Ni, M.; Leung, M. K. H.; Leung, D. Y. C.; Sumathy, K. Renewable & Sustainable Energy Reviews 2007, 11, 401-425.
Lubitz, W.; Reijerse, E. J.; Messinger, J. Energy & Environmental Science 2008, 1, 15-31.
Kudo, A.; Kato, H.; Tsuji, I. Chemistry Letters 2004, 33, 1534-1539.
Chong, D. S.; Georgakaki, I. P.; Mejia-Rodriguez, R.; Samabria-Chinchilla, J.; Soriaga, M. P.; Darensbourg, M. Y. Dalton Transactions 2003, 4158-4163.
Rauchfuss, T. B. Science 2007, 317, 43-43.
Berning, D. E.; Miedaner, A.; Curtis, C. J.; Noll, B. C.; DuBois, M. C. R.; Dubois, D. L. Organometallics 2001, 20, 1832-1839.
DuBois, M. R.; DuBois, D. L. Comptes Rendus Chimie 2008, 11, 805-817.
Jacobsen, G. M.; Shoemaker, R. K.; McNevin, M. J.; DuBois, M. R.; DuBois, D. L. Organometallics 2007, 26, 5003-5009.
Curtis, C. J.; Miedaner, A.; Ciancanelli, R.; Ellis, W. W.; Noll, B. C.; DuBois, M. R.; DuBois, D. L. Inorganic Chemistry 2003, 42, 216-227.
Yang, J. Y.; Bullock, R. M.; Dougherty, W. G.; Kassel, W. S.; Twamley, B.; DuBois, D. L.; DuBois, M. R. Dalton Transactions, 39, 3001-3010.
Yang, J. Y.; Bullock, R. M.; Shaw, W. J.; Twamley, B.; Fraze, K.; DuBois, M. R.; DuBois, D. L. Journal of the American Chemical Society 2009, 131, 5935-5945.
DuBois, D. L.; Bullock, R. M. European Journal of Inorganic Chemistry 2011, 1017-1027.
DuBois, M. R.; DuBois, D. L. Chemical Society Reviews 2009, 38, 62-72.
Pool, D. H.; DuBois, D. L. Journal of Organometallic Chemistry 2009, 694, 2858-2865.
Redin, K.; Wilson, A. D.; Newell, R.; DuBois, M. R.; DuBois, D. L. Inorganic Chemistry 2007, 46, 1268-1276.
Wilson, A. D.; Fraze, K.; Twamley, B.; Miller, S. M.; DuBois, D. L.; DuBois, M. R. Journal of the American Chemical Society 2008, 130, 1061-1068.
Wilson, A. D.; Newell, R. H.; McNevin, M. J.; Muckerman, J. T.; DuBois, M. R.; DuBois, D. L. Journal of the American Chemical Society 2006, 128, 358-366.
Wilson, A. D.; Shoemaker, R. K.; Miedaner, A.; Muckerman, J. T.; DuBois, D. L.; DuBois, M. R. Proceedings of the National Academy of Sciences of the United States of America 2007, 104, 6951-6956.
Frey, M. ChemBioChem 2002, 3, 153-160.
Andzelm, J.; Kolmel, C.; Klamt, A. Journal of Chemical Physics 1995, 103, 9312-9320.
Becke, A. D. Physical Review A 1988, 38, 3098-3100.
Becke, A. D. Journal of Chemical Physics 1993, 98, 5648-5652.

Lee, C. T.; Yang, W. T.; Parr, R. G. Physical Review B 1988, 37, 785-789.
Frisch, A.; Frisch, M. J.; Trucks, G. W. Gaussian 03 user's reference; Gaussian: Carnagie, PA, 2003.
Frisch, M. J.; Trucks, G. W.; Schlegel, H. B.; Scuseria, G. E.; Robb, M. A.; Cheeseman, J. R.; Jr, J. A. M.; Vreven, T.; Kudin, K. N.; Burant, J. C.; Millam, J. M.; Iyengar, S. S.; Tomasi, J.; Barone, V.; Mennucci, B.; Cossi, M.; Scalmani, G.; Rega, N.; Petersson, G. A.; Nakatsuji, H.; Hada, M.; Ehara, M.; Toyota, K.; Fukuda, R.; Hasegawa, J.; Ishida, M.; Nakajima, T.; Honda, Y.; Kitao, O.; Nakai, H.; Klene, M.; Li, X.; Knox, J. E.; Hratchian, H. P.; Cross, J. B.; Bakken, V.; Adamo, C.; Jaramillo, J.; Gomperts, R.; Stratmann, R. E.; Yazyev, O.; Austin, A. J.; Cammi, R.; Pomelli, C.; Ochterski, J. W.; Ayala, P. Y.; Morokuma, K.; Voth, G. A.; Salvador, P.; Dannenberg, J. J.; Zakrzewski, V. G.; Dapprich, S.; Daniels, A. D.; Strain, M. C.; Farkas, O.; Malick, D. K.; Rabuck, A. D.; Raghavachari, K.; Foresman, J. B.; Ortiz, J. V.; Cui, Q.; Baboul, A. G.; Clifford, S.; Cioslowski, J.; Stefanov, B. B.; Liu, G.; Liashenko, A.; Piskorz, P.; Komaromi, I.; Martin, R. L.; Fox, D. J.; Keith, T.; Al-Laham, M. A.; Peng, C. Y.; Nanayakkara, A.; Challacombe, M.; Gill, P. M. W.; Johnson, B.; Chen, W.; Wong, M. W.; Gonzalez, C.; Pople, J. A.; Gaussian, Inc.: Wallingford, CT, 2003.
Takano, Y.; Houk, K. N. Journal of Chemical Theory and Computation 2005, 1, 70-77.
Ginovska, B.; Camaioni, D. M.; Dupuis, M.; Schwerdtfeger, C. A.; Gil, Q. Journal of Physical Chemistry A 2008, 112, 10604-10613.
Klamt, A.; Schuurmann, G. Journal of the Chemical Society-Perkin Transactions 2 1993, 799-805.
Liptak, M. D.; Shields, G. C. Journal of the American Chemical Society 2001, 123, 7314-7319.
Barone, V.; Cossi, M.; Tomasi, J. Journal of Chemical Physics 1997, 107, 3210-3221.
Bondi, A. Journal of Physical Chemistry 1964, 68, 441-&.
Chauvin, R. Journal of Physical Chemistry 1992, 96, 9194-9197.
Rowland, R. S.; Taylor, R. Journal of Physical Chemistry 1996, 100, 7384-7391.
Zhao, X.; Georgakaki, I. P.; Miller, M. L.; Mejia-Rodriguez, R.; Chiang, C. Y.; Darensbourg, M. Y. Inorganic Chemistry 2002, 41, 3917-3928.
Nunes, G. S.; Alexiou, A. D. P.; Araki, K.; Formiga, A. L. B.; Rocha, R. C.; Toma, H. E. European Journal of Inorganic Chemistry 2006, 1487-1495.
Kelly, C. P.; Cramer, C. J.; Truhlar, D. G. Journal of Physical Chemistry B 2006, 110, 16066-16081.
Cukier, R. I.; Nocera, D. G. Annual Review of Physical Chemistry 1998, 49, 337-369.
Meyer, T. J.; Huynh, M. H. V.; Thorp, H. H. Angewandte Chemie-International Edition 2007, 46, 5284-5304.
Small, Y. A.; DuBois, D. L.; Fujita, E.; Muckerman, J. T. Energy & Environmental Science, 4, 3008-3020.

Qi, X. J.; Liu, L.; Fu, Y.; Guo, Q. X. Organometallics 2006, 25, 5879-5886.
Schuurmann, G.; Cossi, M.; Barone, V.; Tomasi, J. Journal of Physical Chemistry A 1998, 102, 6706-6712.
Tissandier, M. D.; Cowen, K. A.; Feng, W. Y.; Gundlach, E.; Cohen, M. H.; Earhart, A. D.; Coe, J. V.; Tuttle, T. R. Journal of Physical Chemistry A 1998, 102, 7787-7794.
Lewis, A.; Bumpus, J. A.; Truhlar, D. G.; Cramer, C. J. Journal of Chemical Education 2004, 81, 596-604.
Short, G. D.; Bishop, E. Analytical Chemistry 1965, 37, 962-&.
Tye, J. W.; Darensbourg, M. Y.; Hall, M. B. Inorganic Chemistry 2006, 45, 1552-1559.
O'Hagan, M.; Shaw, W. J.; Raugei, S.; Chen, S.; Yang, J. Y.; Kilgore, U. J.; DuBois, D. L.; Bullock, R. M. Journal of the American Chemical Society, 133, 14301-14312.
Evans, D. J.; Pickett, C. J. Chemical Society Reviews 2003, 32, 268-275.
Chen, S.; Raugei, S.; Rousseau, R.; Dupuis, M.; Bullock, R. M. Journal of Physical Chemistry A 2011, 114, 12716-12724.
Kanan, M. W.; Surendranath, Y.; Nocera, D. G. Chemical Society Reviews 2009, 38, 109-114.